

An Arbitrary Scale Super-Resolution Approach for 3-Dimensional Magnetic Resonance Image using Implicit Neural Representation

Qing Wu^a, Yuwei Li^a, Yawen Sun^b, Yan Zhou^b, Hongjiang Wei^{c,d}, Jingyi Yu^a, Yuyao Zhang^{a,e,*}

^aSchool of Information Science and Technology, ShanghaiTech University, Shanghai, China

^bDepartment of Radiology, Ren Ji Hospital, School of Medicine, Shanghai Jiao Tong University, Shanghai 200127, P.R. China

^cSchool of Biomedical Engineering, Shanghai Jiao Tong University, Shanghai, China

^dInstitute of Medical Robotics, Shanghai Jiao Tong University, Shanghai, China

^eiHuman Institute, ShanghaiTech University, Shanghai, China

Abstract

High Resolution (HR) medical images provide rich anatomical structure details to facilitate early and accurate diagnosis. In magnetic resonance imaging (MRI), restricted by hardware capacity, scan time, and patient cooperation ability, isotropic 3-dimensional (3D) HR image acquisition typically requests long scan time and, results in small spatial coverage and low signal-to-noise ratio (SNR). Recent studies showed that, with deep convolutional neural networks, isotropic HR MR images could be recovered from low-resolution (LR) input via single image super-resolution (SISR) algorithms. However, most existing SISR methods tend to approach a scale-specific projection between LR and HR images, thus these methods can only deal with a fixed up-sampling rate. For achieving different up-sampling rates, multiple SR networks have to be built up respectively, which is very time-consuming and resource-intensive. In this paper, we propose ArSSR, an *Arbitrary Scale Super-Resolution* approach for recovering 3D HR MR images. In the ArSSR model, the reconstruction of HR images with different up-scaling rates is defined as learning a continuous implicit voxel function from the observed LR images. Then the SR task is converted to represent the implicit voxel function via deep neural networks from a set of paired HR and LR training examples. The ArSSR model consists of an encoder network and a decoder network. Specifically, the convolutional encoder network is to extract feature maps from the LR input images and the fully-connected decoder network is to approximate the implicit voxel function. Due to the continuity of the learned function, a *single* ArSSR model can achieve arbitrary up-sampling rate reconstruction of HR images from any input LR image after training. Experimental results on three datasets show that the ArSSR model can achieve state-of-the-art SR performance for 3D HR MR image reconstruction while using a single trained model to achieve arbitrary up-sampling scales. Code and data for this work are available at: <https://github.com/iwuqing/ArSSR>.

Keywords: MRI, Single Image Super-Resolution, Deep Learning, Implicit Neural Representation.

1. Introduction

Magnetic Resonance Imaging (MRI), as a non-invasive and radiation-free imaging technology, is commonly used for disease detection, diagnosis, and treatment monitoring. High-quality 3-dimensional (3D) high-resolution (HR) MR images provide rich tissue anatomical details, facilitating early-accurate diagnosis and quantitative image analysis. However, limited by the trade-off among image resolution, signal-to-noise

ratio (SNR), and scanning time, it is difficult to acquire high-quality 3D isotropic HR MR images. For example, to increase the image resolution from $2 \times 2 \times 2 \text{ mm}^3$ to $1 \times 1 \times 1 \text{ mm}^3$ requires the average of 64 scans for maintaining a similar SNR, which thus significantly increases scanning time [1, 2]. To alleviate this trade-off, a common and effective strategy is to scan high-SNR low-resolution (LR) MR images and then improve the image resolution via super-resolution (SR) algorithms. A bunch of efficient and powerful SR algorithms has been proposed for this purpose. According to the number of demanded LR MR images [3], SR algorithms can be briefly categorized into multi-image super-resolution

*Corresponding author

Email address: zhangyy8@shanghaitech.edu.cn
(Yuyao Zhang)

(MISR) and single-image super-resolution (SISR). In MISR methods [1, 2, 4, 5], the HR image is generated by combining the high-frequency image information from multiple non-isotropic (i.e. image with high in-plane resolution and thick slices) LR MR images, which are scanned from the same object in different scanning orientations. While SISR methods [6, 7] directly reconstruct the HR image from a single isotropic LR input image without additional scanning. In this paper, we focus our attention on the SISR method category.

Conventional SISR methods include interpolation-based methods and regularization-based methods. Interpolation-based methods, such as cubic/sinc interpolation, often suffer from blocking artifacts due to their poor de-aliasing ability [1]; while regularization-based methods only achieve limited SR performance due to their over-idealistic prior assumptions [8]. Recently, the accuracy of the SISR task has been significantly improved by deep convolutional neural networks (CNNs) due to its non-linearity to learn the mapping between LR images and HR images. A good deal of CNN-based SISR methods [8–14] with well-designed network architectures for 3D MR images have been proposed. However, to the best of our knowledge, most of the existing deep-learning-based methods are designed to deal with the SR tasks of one or several fixed integer up-sampling scales (e.g., $2\times$, $3\times$, and $4\times$). This is mainly because most models tend to approach a scale-specific projection between LR and HR images using deep neural networks. Therefore, these methods have to be respectively trained and stored for each up-sampling scale, which is very computation-expensive and resource-intensive.

In this paper, we propose ArSSR, an *Arbitrary Scale Super-Resolution* model based on implicit neural representation for achieving high-quality 3D HR MR images. In the ArSSR model, the reconstruction of HR images with different up-scaling rates is defined as learning a continuous implicit voxel function from the observed LR images. Then the SR task is converted to represent the implicit voxel function via deep neural networks from a set of paired HR and LR training examples. The ArSSR model consists of an encoder network and a decoder network. Specifically, the convolutional encoder network is to extract feature maps from the LR input images and the fully-connected decoder network is to approximate the implicit voxel function. Due to the continuity of the learned function, a single ArSSR model can reconstruct the HR images with an arbitrary up-sampling rate from any input LR image after training. Figure 1 shows an example of the SISR tasks of

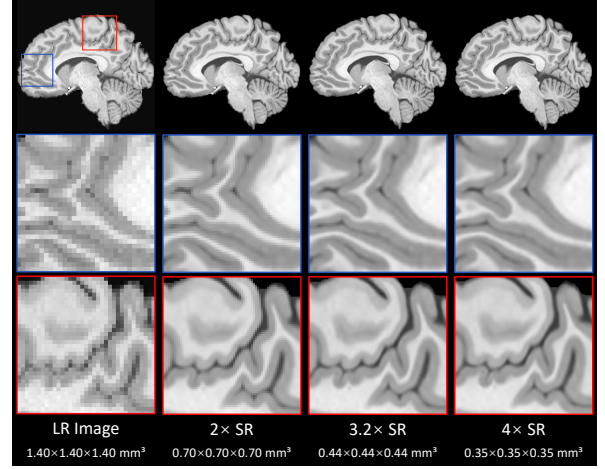


Figure 1: An example of the SISR tasks of three different isotropic up-sampling scales $k = \{2, 3.2, 4\}$ for a 3D brain MR image by the *single* ArSSR model. Note that for isotropic up-sample scale of k , the voxel size reduces by k^3 times, i.e. $2\times$ SR denotes a voxel size of 8 times smaller than before.

different up-sampling rates for a 3D brain MR image by the proposed ArSSR model. It is able to conduct a variety of up-sampling rates including integer rate or non-integer rate. Note that for the isotropic up-sample scale of k , the voxel size reduces by k^3 times, i.e. $2\times$ SR denotes a voxel size of 8 times smaller than before. To comprehensively evaluate the SR performance, we conduct comparison experiments on three different datasets (including two simulation datasets and one real data collection dataset). Both qualitative and quantitative results demonstrate that the proposed ArSSR model can achieve state-of-the-art SR performance for 3D HR MR image reconstruction, while using a single trained model to achieve arbitrary up-sampling scales.

The rest of this paper is organized as follows. Related works are presented in Section 2. Detailed description of ArSSR model is in Section 3. The implementation, experimental settings and results are reported in Section 4. Finally, this work is concluded in Section 5.

2. Related Work

2.1. Single Image Super-Resolution

As a low-level task in computer vision, SISR has received widespread attention for decades [3]. SISR aims to reconstruct the corresponding HR image from a single LR input image. Conventional SISR methods include interpolation-based methods and regularization-based methods. Interpolation-based methods, such as cubic/sinc interpolation, are widely used due to their

computational simplicity, but they often introduce severe blocking artifacts [1, 15]. Regularization-based methods [6, 16] recover the desired HR image by solving a convex optimization problem. Since the SISR task is a severely ill-posed problem (i.e., there exist multiple HR solutions for a single LR input image), regularization-based methods usually adopt over-idealistic yet sophisticated prior assumptions to restrict the possible solution space. However, those prior assumptions do not always hold, which may greatly limit the SR performance of the models. For example, total variation [16] supposes that the optimal HR image should be constant in a small neighborhood, which is inconsistent with the fact in some regions (e.g., brain cerebellum) of the HR images that have abundant local details.

Recently, deep learning methods have shown great potential in the SISR task. Dong et al. [17, 18] proposed super-resolution convolutional neural network (SRCNN), which is the first deep-learning-based SISR model. SRCNN directly learns the optimal mapping between LR images and HR images from a large amount of training examples using an end-to-end way thus it achieves great performance improvement compared with the traditional interpolation- and regularization-based SISR models. After that, many deep-learning-based SISR models [19–26] with more complicated network structures have been proposed. For instance, Kim et al. [20] developed a very deep convolutional network (VDSR) by increasing the network depth and utilizing residual connections. Ledig et al. [21] proposed a super-resolution generative adversarial network (SRGAN). Due to the perceptual loss function consist of an adversarial loss and a content loss, SRGAN is able to reconstruct photo-realistic natural images for $4\times$ up-sampling scale.

Following the rapid development of deep learning networks in the SISR task of 2D natural images, many SR model have been adopted to the SISR task for 3D medical images. Pham et al. [9] successfully reconstructed high-quality 3D HR MR brain images by SRCNN3D, a 3D version of the SRCNN [17, 18]. Chen et al. [10] developed a densely connected super-resolution network (DCSRN) by incorporating dense connections. Du et al. [11] proposed a 20-layers residual convolutional neural network (ResCNN) by increasing the network depth and using residual connections. Chen et al. [13] developed mDCSRN-GAN, the first generative adversarial SR network for 3D MR images. Benefiting from the well-designed network structures, all these models achieved satisfying SR performance. Yet, due to the fact that these models regard the SISR of differ-

ent up-sampling scales as independent tasks, they have to be trained and stored for each up-sampling scale, respectively. Different from previous works, the proposed ArSSR model considers the SISR with arbitrary up-sampling scales as a single task. Therefore, the single fine-trained ArSSR model can conduct the SISR tasks of arbitrary scales, which greatly improves the practical applicability.

2.2. Implicit Neural Representation

In the real world, most of the visual signals can be considered as continuous functions of a certain dimensional variables. For instance, a 2D natural image can be modeled by a continuous function of 2D pixel coordinates; a 3D MR/CT image can be modeled by a continuous function of 3D voxel coordinates. However, conventional signal representations are usually discrete (e.g., pixel-based representations for 2D images and voxel-based representations for 3D MR/CT images) due to the digital computational system, which results in a severe trade-off between the accuracy of the represented signals and the storage resources. To alleviate this problem, implicit neural representation (INR) recently has emerged [27–29] as a novel way for continuously parametrizing a variety of signals. In the INR, a represented signal is modeled by a pre-defined continuous function that maps spatial coordinates to the signal responses. Then, the function is approximated by a simple fully connected network (i.e., an MLP). Once the function is approached well, the MLP theoretically can estimate the signal response at any given position. Therefore, the INR is continuous and independent of the signal resolution.

The INR initially was proposed in these three works [27–29] for 3D shape and surface modeling. Chen et al. [27] proposed an implicit field decoder that greatly improves the visual quality of generative shape modeling by concatenating point coordinates with shape features, feeding both as input to the implicit decoder; Jeong et al. [28] developed a continuous deep signed distance function that can enable the representation of complex shapes with small memory without discretization errors; Mescheder et al. [29] proposed an occupancy network, in which a 3D surface is modeled as the continuous decision boundary of a deep neural network classifier and thus the 3D surface at infinite resolution can be accurately encoded with limited memory footprint. The three works firstly demonstrated that the INR greatly outperforms grid-, point-cloud-, and mesh-based representation for 3D surface and shape modeling. Since then, a number of INR-based models [30–35] for 3D shape and surface have been proposed. In the field of

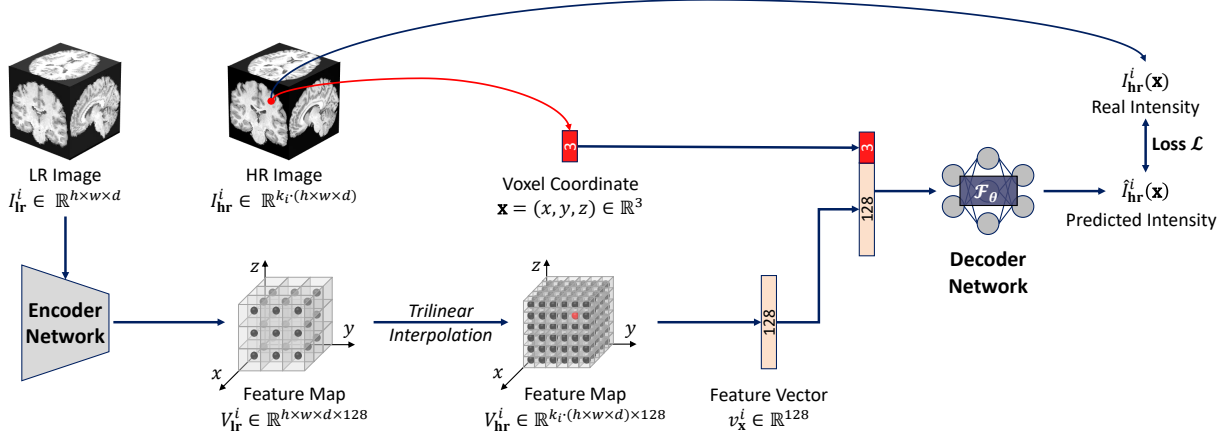


Figure 2: An overview of the proposed ArSSR model.

2D natural images, Chen et al. [36] proposed a local implicit image function trained by a self-supervised SR task that is theoretically able to recover HR images of arbitrary resolutions from a single LR input image; Lin et al. [37] developed InfinityGAN model for infinite-resolution image synthesis; Tang et al. [38] proposed a novel joint implicit image function by formulating the guided SR task as a neural implicit image interpolation problem. Inspired by these works, we propose ArSSR, the first INR-based arbitrary scale SISR model for 3D MR images. The single ArSSR model can conduct SISR tasks of arbitrary up-sampling scales by learning a novel implicit voxel function.

3. Methodology

3.1. Problem Modeling

In our previous work [39], we suppose that the desired HR image I_{hr} and the observed LR image I_{lr} can be modeled via a same implicit function as defined below:

$$I = f_\theta(\mathbf{x}) \quad (1)$$

where $\mathbf{x} = (x, y, z)$ denotes any 3D voxel spatial coordinate, and I denotes the voxel intensity at the coordinate \mathbf{x} in the image. The pair of HR and LR images are considered as the explicit representation of the implicit function $f_\theta(\mathbf{x})$ with different sampling rate. In the HR image I_{hr} , more voxels are included than that in the LR image I_{lr} . As we suppose the function $f_\theta(\mathbf{x})$ is continuous with the spatial coordinate system \mathbf{x} , once the

function is well approached, an arbitrary up-sampling scale for the LR image can be achieved.

However, it is impractical to train a specific function $f_\theta(\mathbf{x})$ for each image. Instead, we are eager to find a more flexible implicit function that is able to represent each pair of LR and HR images in the SR task. Towards this end, we propose a novel implicit voxel function \mathcal{F}_θ , which is expressed as below:

$$I^i = \mathcal{F}_\theta(\mathbf{x}, v_{\mathbf{x}}^i) \quad (2)$$

where $v_{\mathbf{x}}^i \in \mathbb{R}^{128}$ denotes a latent space feature vector for the voxel intensity at the spatial coordinate \mathbf{x} in image I^i . The vector is extracted using a SR task-specific convolutional encoder. Instead of simply representing an image via spatial system, variable of \mathcal{F}_θ includes both coordinate and intensity embedding features of the MR images to be reconstructed. By combining convolutional encoders with implicit function decoders, our model is able to integrate local image intensity information, thus substantially improves the ability of the implicit decoder to represent and recover fine image details when scaling to any finer image resolution.

3.2. Model Overview

An overview of the proposed ArSSR model is illustrated in Figure 2. For a given pair of LR-HR images from the training set $\mathbf{I} = \{I_{lr}^i \in \mathbb{R}^{h \times w \times h}, I_{hr}^i \in \mathbb{R}^{k_i \cdot (h \times w \times h)}\}_{i=1}^M$, where M is the number of training examples and k_i is the up-sampling scale for the i -th pair of LR-HR images, we first use a convolutional encoder network to convert LR image I_{lr}^i into a feature map $V_{lr}^i \in \mathbb{R}^{h \times w \times d \times 128}$, where each element

is a feature vector $v_{\mathbf{x}}^i \in \mathbb{R}^{128}$ for the corresponding voxel at the coordinate \mathbf{x} in the LR image I_{lr}^i . Then, for any query of 3D voxel coordinate $\mathbf{x} = (x, y, z)$ from the HR image I_{hr}^i , we generate its feature map $V_{\text{hr}}^i \in \mathbb{R}^{k_i \cdot (h \times w \times d) \times 128}$ by trilinear interpolating on the LR image feature map V_{lr}^i . Finally, the decoder network takes the query coordinate \mathbf{x} and the corresponding feature vector $v_{\mathbf{x}}^i$ in the feature map V_{hr}^i as input, and outputs the voxel intensity $\hat{I}_{\text{hr}}^i(\mathbf{x})$ at the spatial coordinate \mathbf{x} . By using back-propagating gradient decent algorithm [40] to minimize the L1 loss function \mathcal{L} between the predicted voxel intensity $\hat{I}_{\text{hr}}^i(\mathbf{x})$ and the real voxel intensity $I_{\text{hr}}^i(\mathbf{x})$, the encoder and decoder network can be optimized simultaneously. Formally, The L1 loss function \mathcal{L} is expressed as follows:

$$\mathcal{L} = \frac{1}{N \times \mathcal{K}} \sum_{i=1}^N \sum_{j=1}^{\mathcal{K}} |I_{\text{hr}}^i(\mathbf{x}_j) - \hat{I}_{\text{hr}}^i(\mathbf{x}_j)| \quad (3)$$

where N denotes the number of the HR-LR image pairs and \mathcal{K} denotes the number of the coordinates sampled from each HR image I_{hr}^i during each training iteration.

After the model training, the encoder network acts as a feature map extractor and the decoder network is an approximator of the implicit voxel function \mathcal{F}_{θ} . For any unknown LR image $I_{\text{lr}} \in \mathbb{R}^{h \times w \times d}$, we firstly use the encoder network to extract its feature map $V_{\text{lr}} \in \mathbb{R}^{h \times w \times d \times 128}$, and then we build a more dense coordinate grid for generating a HR image $I_{\text{hr}} \in \mathbb{R}^{H \times W \times D}$, where $[H, W, D] = k \cdot [h, w, d]$ and k is an arbitrarily up-sampling scale, with higher sampling rate on the implicit image function. The feature map $V_{\text{hr}} \in \mathbb{R}^{H \times W \times D \times 128}$ for the HR image is synthesized via trilinear interpolating on the LR image feature map V_{lr} . And afterwards we can use the decoder network to predict voxel intensity $I_{\text{hr}}(\mathbf{x})$ at any spatial coordinate in the reconstructed HR image grid. Thus the HR image I_{hr} with an arbitrary spatial resolution can be achieved.

3.3. Encoder Network

In pioneering works [27–29] that represent 3D surfaces using implicit neural representation, a general and efficient strategy is to encode input signals (e.g., volume data, point cloud) into a single latent vector by a encoder network. However, this strategy does not integrate local information in the input signals as claimed in [30, 36], so these models cannot finely represent the 3D surfaces with complex shapes. To this end, Peng et al. [30] developed a convolutional occupancy network that conduct elements-wise feature extraction for the input signals, which greatly improve the performance for

3D surface reconstruction. Meanwhile, Chen et al. [36] proposed a local implicit image function for representing 2D natural images, which can recover HR images with an arbitrary resolution from an unknown LR image.

Inspired by the works [30, 36], we use an encoder network to extract voxel-wise latent space feature vector for the LR images. The encoder network takes the LR image $I_{\text{lr}}^i \in \mathbb{R}^{h \times w \times d}$ as input and outputs a feature map $V_{\text{lr}}^i \in \mathbb{R}^{h \times w \times d \times 128}$, where each element is a feature vector $v_{\mathbf{x}}^i \in \mathbb{R}^{128}$ for the corresponding voxel at the coordinate \mathbf{x} in the LR image I_{lr}^i . This voxel-wise latent space extraction strategy facilitates the following decoder network to efficiently integrate local image intensity information and thus successfully recover fine image details in the HR image at even a large up-sampling scale.

We apply a modified residual dense network (RDN) [23] to implement our encoder network. In particular, we remove the upscaling layer in the original RDN, extent all the 2D convolutional layers to 3D convolutional layers, and set the output channel number of the last layer as 128. The number of the residual dense blocks (RDBs) is 8 and each RDB has 3 3D convolutional layers. The growth rate of RDBs is set to 64. Note that our encoder network can be replaced by any other SR network without upscaling layer. In the experiment section, the effect of the encoder network are discussed.

3.4. Decoder Network

After the encoder network, the LR image I_{lr}^i is converted to the feature map V_{lr}^i . Our decoder network aims to approximate the implicit voxel function \mathcal{F}_{θ} and thus is able to estimate the HR image voxel intensities $\hat{I}_{\text{hr}}^i(\mathbf{x})$ at any spatial coordinate \mathbf{x} . Specifically, as HR image involves much more voxels than that in the input LR image, we need to fill the gaps for the enlarging number of feature vector $v_{\mathbf{x}}^i$. Thus given any query of 3D voxel coordinate \mathbf{x} from the HR image I_{hr}^i , we generate its feature map V_{hr}^i by trilinear interpolating the feature map V_{lr}^i that converted from the LR image I_{lr}^i , as shown in Figure 3. Formally, the feature vector $v_{\mathbf{x}}^i$ is calculated as:

$$v_{\mathbf{x}}^i = \sum_{k=0}^7 \frac{S_k}{S} \cdot v_k^i, \quad S = \sum_{k=0}^7 S_k \quad (4)$$

where v_k^i ($k = 0, \dots, 7$) are the nearest 8 feature vectors of the query coordinate \mathbf{x} in the feature map V_{lr}^i , S_k is the volume of the cuboid between the query coordinate \mathbf{x} and the coordinate diagonal to the feature vector v_k^i . Then, the decoder network takes each query voxel

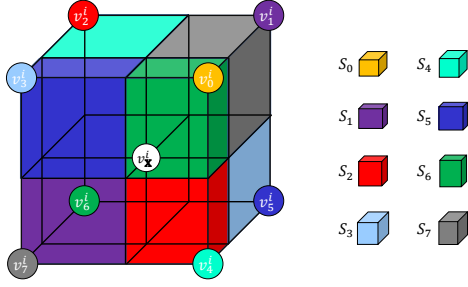


Figure 3: For any 3D voxel coordinate \mathbf{x} , we query the nearest 8 feature vectors v_k^i ($k = 0, 1, \dots, 7$) in the feature map V_{hr}^i , then generate the corresponding feature vectors $v_{\mathbf{x}}^i$ in the feature map V_{hr}^i according to Equ 4.

coordinate \mathbf{x} and the feature vector $v_{\mathbf{x}}^i$ as input, and finally outputs the estimated voxel intensity $\hat{I}_{\text{hr}}^i(\mathbf{x})$ at the coordinate \mathbf{x} .

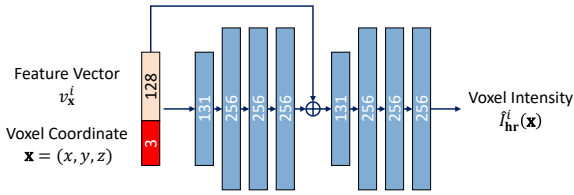


Figure 4: Architecture of the decoder network. The decoder network takes a query voxel coordinate $\mathbf{x} = (x, y, z) \in \mathbb{R}^3$ and the corresponding feature vectors $v_{\mathbf{x}}^i$ in the feature map V_{hr}^i as input, and outputs the voxel intensity $\hat{I}_{\text{hr}}^i(\mathbf{x})$ at that spatial coordinate \mathbf{x} .

Figure 4 illustrates the architecture of the decoder network. It consists of 8 standard fully-connected layers. Each layer is followed by a ReLU activation layer [41]. To facilitate the training process, we involve a residual connection [42] between the input layer and the 4th’s ReLU activation layer. And except that there are 131 neurons in the 1st and 4th full-connected layers, all other full-connected layers have 256 neurons.

4. Experiments

In order to comprehensively evaluate the proposed ArSSR model, we conduct the following five experiments:

1. *The SISR Tasks on HCP-1200 Dataset* [43]. The ArSSR model and four baseline models (Cubic interpolation and three most-cited deep-learning-based MRI

SISR models [9–11]) are trained on training set and validation set of the Human Connectome Projection (HCP-1200) Dataset [43]. Then, on testing set of the HCP-1200 dataset [43], these well-trained models are used to conduct the SISR tasks of five isotropic up-sampling scales $k = \{2, 2.5, 3, 3.5, 4\}$. Specially, for an isotropic up-sampling scale of k , the voxel size reduces by k^3 times, which is very challenging task. For example, to perform a $4\times$ SR denotes to generate an image with voxel size of 64 times smaller than that before the SR process. Both the qualitative and quantitative results are reported. It is worth to notice that for the ArSSR, we train one model for achieving the five up-sampling scales; while for the other three deep-learning-based baselines, we train a model for each up-sampling scale, *respectively*.

2. *The SISR Tasks on Lesion Brain Dataset*. To further compare the generalization ability between the ArSSR model and baseline methods, all the well-trained models are used to perform the SISR tasks of three isotropic up-sampling scales $k = \{2, 3, 4\}$ on the Lesion Brain dataset. Similarly, we also report the qualitative and quantitative results. Note that here all models are trained on the HCP-1200 dataset [43] without any fine-tuning before testing on other dataset.

3. *The SISR Tasks on Healthy Brain Dataset*. To test the performance of the ArSSR and the baseline models in real MR image scanning scenario, we use cubic interpolation, ResCNN, and the ArSSR to conduct the SISR tasks of three isotropic up-sampling scales $k = \{2, 3, 4\}$ on the Healthy Brain dataset, which is a real collected dataset. We qualitatively demonstrate the difference between the SISR results and reference images. Note that here ResCNN [11] and the ArSSR model are trained on the HCP-1200 dataset [43] without any fine-tuning before testing on other dataset.

4. *Fully Automatic Segmentation based Evaluation*. To further evaluate the quality of the SISR results, we follow the segmentation evaluation strategy as in previous works [8, 44]. In particular, we adopt Ants (<http://stnava.github.io/ANTs/>), an open-sources medical image processing toolkit, to conduct a fully automatic segmentation on the SR results by all the compared models on the testing set of the HCP-1200 dataset [43]. The quality of the SISR images can be further verified by qualitatively and quantitatively analyzing the differences between the segmentation results of the SISR images and the GT images.

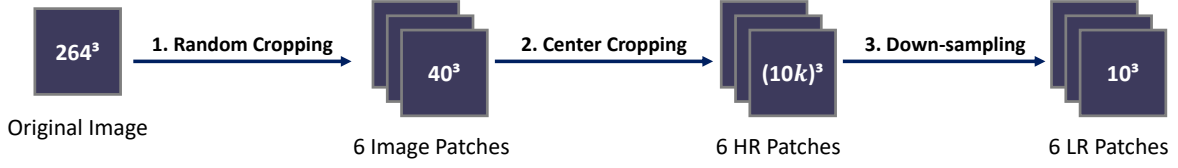


Figure 5: A pipeline of data preprocessing for the training set and validation set of the HCP-1200 dataset [43]. For the three deep learning-based models, the scales $k = \{2, 2.5, 3, 3.5, 4\}$; while for our ArSSR model, the scale k is randomly sampled from uniform distribution $\mathcal{U}(2, 4)$. The LR-HR patch pairs are used to train the models.

5. Stability Analysis for the ArSSR Model. On the HCP-1200 dataset [43], we investigate the effect of using different encoder network, to test the stability of ArSSR model. In particular, we employ three different CNN structures (including ResCNN [11], SRResNet [21], and RDN [23]) to implement the encoder network, and then qualitatively and quantitatively compare the performance of the ArSSR models with three different encoder networks for the SISR task of five isotropic up-sampling scales $k = \{2, 2.5, 3, 3.5, 4\}$. Besides, the curves of training error and validation error with epochs are reported.

4.1. Experimental Settings

4.1.1. Datasets & Preprocessing

All experiments are conducted on three datasets: HCP-1200 dataset [43], Lesion Brain dataset, and Healthy Brain dataset. the HCP-1200 dataset [43] and Lesion Brain dataset are simulation datasets, where the LR images are simulated by downsampling the corresponding HR images; while Healthy Brain dataset is a real collected dataset, where LR and HR images are collected from the same subject using different image scanning protocols on a 3T MR scanner.

HCP-1200 Dataset. The HCP-1200 dataset [43] is a large public human brain MR image dataset, which consists of 1113 3D isotropic HR T1-weighted brain MR images. These HR T1-weighted MR images were acquired on Siemens 3T platforms using a 32-channel head coil. MPAGE sequences were used with following parameters: repetition time (TR) = 2400 ms; echo time (TE) = 2.14 ms; field of view (FOV) = $224 \times 224 \text{ mm}^2$; matrix size = 320×320 ; slice thickness = 0.7 mm; 256 continuous sagittal slices; voxel size = $0.7 \times 0.7 \times 0.7 \text{ mm}^3$.

In our experiments, the HCP-1200 dataset is split into three parts: 780 images for training set, 111 ones in validation set, and 222 ones in testing set. Note that the testing set is only used for final performance evaluation

and no images are overlapped in the three parts. Additionally, we apply cropping and padding to all the original images to modify the image dimension size from $320 \times 320 \times 256$ to $264 \times 264 \times 264$ for the convenience of quantitative evaluations. For the testing set, we use the original MR images as ground truth (GT) HR images, and then downsample the GT images by cubic interpolation at the specific down-sampling scales $k = \{2, 2.5, 3, 3.5, 4\}$ to simulate the LR images, and thus the testing set is prepared. For the training and validation set, we follow the pipeline of the data preprocessing in the prior work [36], which is shown in Figure 5. For an original image, we first apply random cropping to extract 6 image patches of a 40^3 dimension size, and then conduct center cropping to generate HR patches of a $(10 \times k)^3$ dimension size. Finally, we downsample the HR patches by cubic interpolation to simulate the LR patches of a 10^3 dimension size. For the proposed ArSSR model, the scale k is randomly sampled from uniform distribution $\mathcal{U}(2, 4)$.

Lesion Brain Dataset. Seventeen T1-weighted brain MR images are acquired from 17 patients with cerebrovascular disease (CVD) on a 3T GE scanner with 8-channel head coil. MPAGE sequences were used with following parameters: TR = 5.5 ms; TE = 1.7 ms; flip angle = 15° ; matrix size = 256×256 ; slice thickness = 1 mm; 156 continuous sagittal slices; voxel size = $1 \times 1 \times 1 \text{ mm}^3$. The current study was approved by the Research Ethics Committee of Ren Ji Hospital and School of Medicine, Shanghai Jiao Tong University, China.

In our experiments, the Lesion Brain dataset is only used as a testing dataset for evaluating the ability of proposed method on recovering HR image with unknown image detail (i.e. brain tissue lesion pattern). All included images comprise of brain tissue lesions in white matter (WM), which have never been seen during the model training procedure. We use the original images as GT images, and then downsample the GT images by cubic interpolation with the specific down-sampling scales

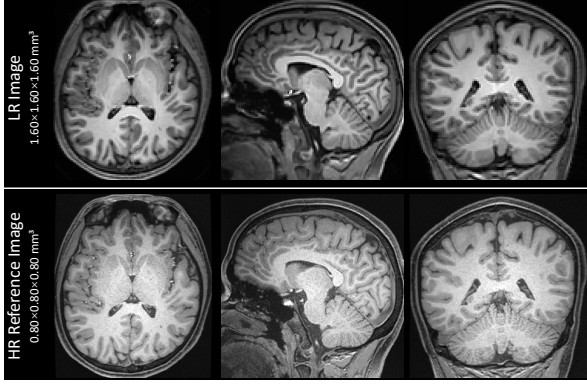


Figure 6: Qualitative comparison of LR image and HR reference image from the Healthy Brain dataset. LR image has a spatial resolution of $1.6 \times 1.6 \times 1.6 \text{ mm}^3$, scanning time ≈ 3 minutes; reference image has a spatial resolution of $0.8 \times 0.8 \times 0.8 \text{ mm}^3$, scanning time ≈ 11 minutes.

$k = \{2, 3, 4\}$ to simulate the LR images.

Healthy Brain Dataset. We scan two T1-weighted brain MR images from the same healthy adult volunteer on a 3T United Imaging MR scanner. As shown in Figure 6, the first row is a LR image with high SNR, while the second row is a HR image with low SNR. The LR image was acquired by MPRAGE sequence with the following parameters: TR = 6.70 ms; TE = 3.0 ms; flip angle = 8° ; matrix size = 160×150 ; slice thickness = 1.6 mm; 104 continuous sagittal slices; voxel size = $1.6 \times 1.6 \times 1.6 \text{ mm}^3$; scanning time ≈ 11 minutes. The HR image was acquired by sequence with the following parameters: TR = 8.07 ms; TE = 3.4 ms; flip angle = 8° ; matrix size = 320×300 ; slice thickness = 0.8 mm; 208 continuous sagittal slices; voxel size = $0.8 \times 0.8 \times 0.8 \text{ mm}^3$; scanning time ≈ 3 minutes. This data collection was approved by the Ethics Committee of ShanghaiTech University.

In our experiments, we employ the LR image as the input image for the models and the HR image as the reference image.

4.1.2. Quality Evaluation Metrics

To quantitatively evaluate the performance of all the models for the SISR task comparison, we adopt five objective image quality metrics. First, we first compute Peak Signal-to-Noise Ratio (PSNR), which is defined as follows:

$$\text{PSNR}(I_{\text{sr}}, I_{\text{gt}}) = 20 \times \log_{10} \left[\frac{L}{\text{MES}(I_{\text{sr}}, I_{\text{gt}})} \right] \quad (5)$$

where I_{sr} and I_{gt} are the reconstructed image and reference image, respectively. And $\text{MES}(I_{\text{sr}}, I_{\text{gt}}) = \sqrt{\frac{1}{N} \sum_{i=1}^N |I_{\text{sr}}(i) - I_{\text{gt}}(i)|}$. N is the number of the voxels in reference image I_{gt} and L is the maximum voxel intensity in the reference image I_{gt} (In our experiment, $L = 1$). The second metric is Structural Similarity Index Measure (SSIM) [45], which is expressed as follows:

$$\text{SSIM}(I_{\text{sr}}, I_{\text{gt}}) = \frac{(2\mu_{\text{sr}}\mu_{\text{gt}} + c_1) \times (\sigma_{\text{sr,gt}} + c_2)}{(\mu_{\text{sr}}^2 + \mu_{\text{gt}}^2 + c_1) \times (\sigma_{\text{sr}}^2 + \sigma_{\text{gt}}^2 + c_2)} \quad (6)$$

where μ_{sr} and μ_{gt} are the means of all the pixels in I_{sr} and I_{gt} , σ_{sr} and σ_{gt} are the variances of all the pixels in I_{sr} and I_{gt} , $\sigma_{\text{sr,gt}}$ is the covariance of I_{sr} and I_{gt} , c_1 and c_2 are relaxation constants.

PSNR and SSIM [45] are widely adopted for quantitative evaluation of the SISR models. However, the recent works [13, 21, 44, 46] demonstrated that the two metrics cannot represent image visual quality well (e.g., an over-smoothed SISR result with extreme loss on the fine image details may score high on the two metrics). Therefore, we also conduct LPIPS [46], a deep-learning-based perceptual similarity measure for quantitative evaluation. By comprehensive experiments, Zhang et al. [46] proved that compared with the pixel-wise metrics like PSNR and NMSE, the LPLPS represent image visual quality more realistically. Additional, another two non-referenced quality metrics (PSI [47] and LPC-SI [48]) are also calculated. LPIPS [46], PSI [47], and LPC-SI [48] are exclusively designed for 2D images, while the MR images discussed in this paper are in 3D. Thus we use the slice-by-slice strategy to compute them. Specifically, all the three metrics are calculated in three steps: Given a 3D MR image, we first extract its 2D MR slices from three orthogonal directions (Axial, Sagittal, and Coronal direction). Then, we compute the scores for each 2D MR slice. Finally, we average the scores of all the 2D MR slices to calculate the final scores.

4.1.3. Training Details

For the training of the ArSSR model, in each step of training, we first randomly sample 15 LR-HR patch pairs (i.e., $N = 15$ in Equ. 3) from the training set, and then we randomly sample 8000 voxel coordinates (i.e., $\mathcal{K} = 8000$ in Equ. 3) from each HR patch as the inputs of the decoder network. We use Adam optimizer [49] to minimize the L1 loss function and the hyperparameters of the Adam are set as follows: $\beta_1 = 0.9$, $\beta_2 = 0.999$, $\epsilon = 10^{-8}$. The learning rate starts from 10^{-4}

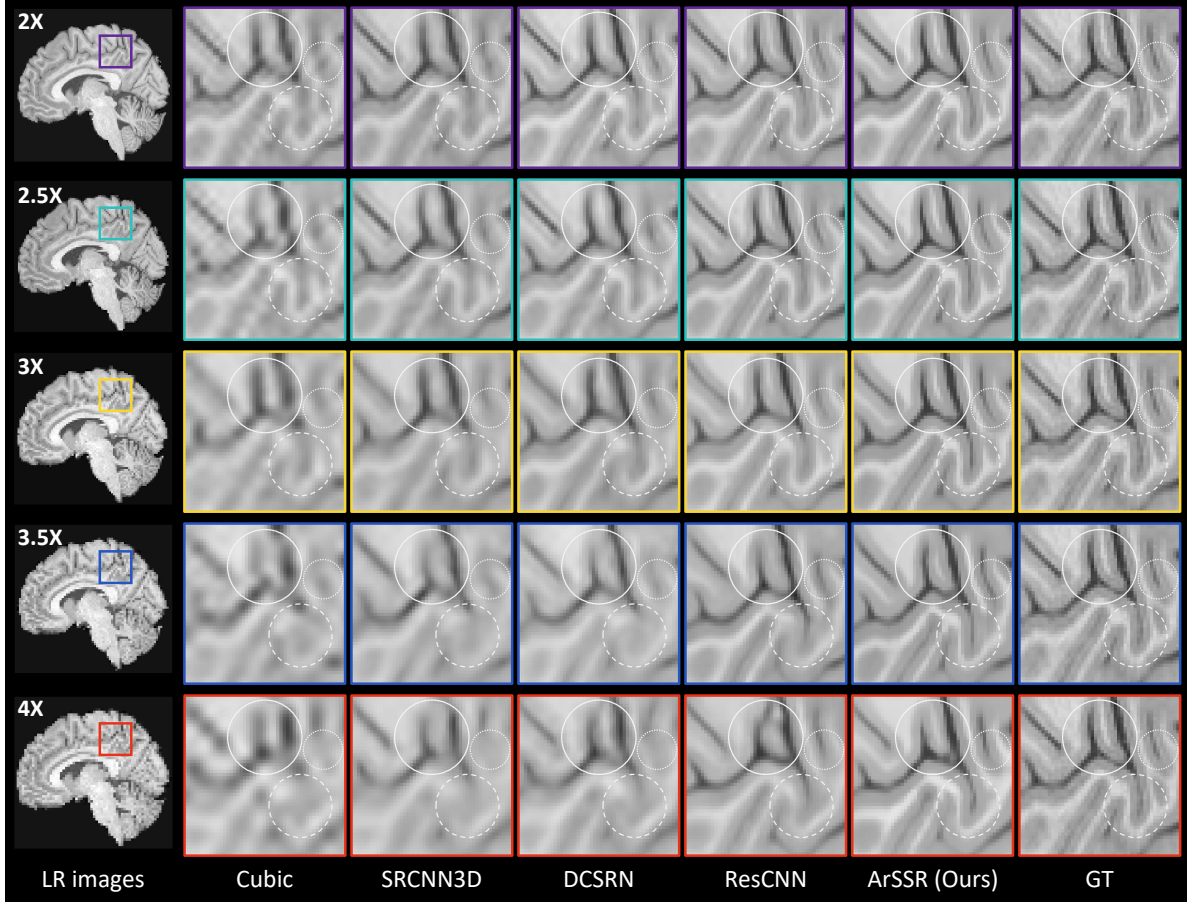


Figure 7: Qualitative comparison of all the compared models on a representative testing sample (No. #827052) from the testing set of the HCP-1200 dataset [43] for the SISR tasks of five isotropic up-sampling scales $k = \{2, 2.5, 3, 3.5, 4\}$. Note that SRCNN3D [9], DCSRNN [10], and ResCNN [11] are *respectively* trained and tested for each scale; while a *single* ArSSR (Ours) model is trained and tested for the five scales.

and decays by factor 0.5 every 200 epochs. The total number of training epochs is 2500, which takes about 12 hours on a single NVIDIA TITAN RTX 24G GPU. The best model is saved by checkpoints during the training.

4.1.4. Baseline Methods

We adopt cubic interpolation and three popular deep-learning-based SISR models (including SRCNN3D [9], DCSRNN [10], and ResCNN [11]) for 3D MR images as baseline methods. Cubic interpolation is implemented by the scipy library [50] of Python, while the three deep-learning-based models are implemented by Pytorch deep learning framework (<https://pytorch.org/>) following the original papers. For the three models, we employ Adam optimizer [49] to train them through back propagation algorithm with a mini-batch size of 10, and the hyper-parameters of the

Adam optimizer [49] are set as follows: $\beta_1 = 0.9$, $\beta_2 = 0.999$, and $\varepsilon = 10^{-8}$. The learning rate is initialized as 10^{-4} and decays by factor 0.5 every 200 epochs. The total number of training epochs is 2000 and the best models are saved by checkpoints during the training.

4.2. Results & Discussion

4.2.1. The SISR Tasks on the HCP-1200 Dataset

For the SISR tasks of five isotropic up-sampling scales $k = \{2, 2.5, 3, 3.5, 4\}$, we train the ArSSR and the four baseline methods on the training set and validation set of the HCP-1200 dataset [43] and then test them on the testing set of the HCP-1200 dataset [43]. Due to the fact that SRCNN [9], and DCSRNN [10], and ResCNN [11] consider the SISR of different scales as independent tasks, they have to be trained and tested *respectively* for each scale. Therefore, for the three baseline models, we totally train 15 independent models for

Scales	Models	Reference-based Metrics			Non-reference-based Metrics	
		PSNR \uparrow	SSIM \uparrow	LPIPS \downarrow	PSI \uparrow	LCP-SI \uparrow
2 \times	Cubic	24.44 \pm 2.85	0.9553 \pm 0.0120	0.0954 \pm 0.0171	0.2978 \pm 0.0084	0.9359 \pm 0.0097
	SRCNN3D	38.11 \pm 2.22	0.9764 \pm 0.0061	0.0634 \pm 0.0150	0.2959 \pm 0.0102	0.9372 \pm 0.0104
	DCSRN	38.50 \pm 2.20	0.9783 \pm 0.0058	0.0540 \pm 0.0129	0.3125 \pm 0.0109	0.9400 \pm 0.0095
	ResCNN	39.58 \pm 2.34	0.9824 \pm 0.0055	0.0371 \pm 0.0119	0.3355 \pm 0.0127	0.9474 \pm 0.0085
	ArSSR (Ours)	36.55 \pm 2.17	0.9700 \pm 0.0066	0.0549 \pm 0.0157	0.3083 \pm 0.0118	0.9435 \pm 0.0091
2.5 \times	Cubic	23.28 \pm 2.85	0.9389 \pm 0.0136	0.1565 \pm 0.0251	0.2560 \pm 0.0057	0.9289 \pm 0.0104
	SRCNN3D	36.01 \pm 2.16	0.9613 \pm 0.0086	0.1001 \pm 0.0199	0.2666 \pm 0.0090	0.9301 \pm 0.0128
	DCSRN	35.96 \pm 2.13	0.9287 \pm 0.0083	0.0992 \pm 0.0177	0.2722 \pm 0.0097	0.9360 \pm 0.0118
	ResCNN	37.20 \pm 2.25	0.9665 \pm 0.0078	0.0621 \pm 0.0166	0.3315 \pm 0.0131	0.9465 \pm 0.0093
	ArSSR (Ours)	34.57 \pm 2.11	0.9538 \pm 0.0087	0.0715 \pm 0.0187	0.3089 \pm 0.0120	0.9428 \pm 0.0095
3 \times	Cubic	22.54 \pm 3.13	0.9268 \pm 0.0171	0.2196 \pm 0.0271	0.2182 \pm 0.0044	0.9224 \pm 0.0112
	SRCNN3D	35.00 \pm 2.12	0.9506 \pm 0.0096	0.1303 \pm 0.0213	0.2269 \pm 0.0081	0.9243 \pm 0.0149
	DCSRN	35.41 \pm 2.14	0.9523 \pm 0.0094	0.1168 \pm 0.0192	0.2507 \pm 0.0085	0.9314 \pm 0.0127
	ResCNN	35.98 \pm 2.18	0.9622 \pm 0.0086	0.0876 \pm 0.0184	0.2741 \pm 0.0109	0.9408 \pm 0.0106
	ArSSR (Ours)	33.42 \pm 2.07	0.9426 \pm 0.0092	0.0811 \pm 0.0188	0.2986 \pm 0.0123	0.9426 \pm 0.0099
3.5 \times	Cubic	21.95 \pm 2.77	0.9120 \pm 0.0176	0.2765 \pm 0.0263	0.1938 \pm 0.0042	0.9115 \pm 0.0120
	SRCNN3D	33.76 \pm 2.10	0.9341 \pm 0.0114	0.1643 \pm 0.0215	0.1904 \pm 0.0065	0.9156 \pm 0.0176
	DCSRN	33.60 \pm 1.95	0.7558 \pm 0.0104	0.1537 \pm 0.0192	0.2108 \pm 0.0083	0.9263 \pm 0.0150
	ResCNN	34.30 \pm 2.19	0.9466 \pm 0.0108	0.1160 \pm 0.0201	0.2707 \pm 0.0122	0.9396 \pm 0.0112
	ArSSR (Ours)	31.98 \pm 2.04	0.9242 \pm 0.0106	0.1009 \pm 0.0212	0.2798 \pm 0.0115	0.9405 \pm 0.0111
4 \times	Cubic	21.33 \pm 3.20	0.9037 \pm 0.0179	0.3252 \pm 0.0263	0.1729 \pm 0.0035	0.9062 \pm 0.0138
	SRCNN3D	33.24 \pm 2.10	0.9261 \pm 0.0121	0.1881 \pm 0.0211	0.1675 \pm 0.0055	0.9116 \pm 0.0196
	DCSRN	33.52 \pm 2.08	0.9175 \pm 0.0116	0.1714 \pm 0.0183	0.2007 \pm 0.0092	0.9242 \pm 0.0179
	ResCNN	33.86 \pm 2.17	0.9383 \pm 0.0108	0.1389 \pm 0.0212	0.2349 \pm 0.0101	0.9342 \pm 0.0124
	ArSSR (Ours)	31.33 \pm 2.03	0.9155 \pm 0.0107	0.1136 \pm 0.0215	0.2534 \pm 0.0090	0.9394 \pm 0.0114

Table 1: Quantitative results of all the compared models on the testing set of the HCP-1200 dataset [43] for the SISR tasks of the five isotropic up-sampling scales $k = \{2, 2.5, 3, 3.5, 4\}$. Note that SRCNN3D [9], DCSRNN [10], and ResCNN [11] are *respectively* trained and tested for each scale; while a *single* ArSSR (Ours) model is trained and tested for the five scales. The symbol \uparrow means that the higher score, the better image quality; while the symbol \downarrow indicates that the lower score, the better image quality. The best and second performance are highlighted in **red** and **blue**, respectively.

the five scales, which in practice is very time-consuming and resource-intensive. While for the ArSSR model, we train a *single* model for the five scales on a continuous interval $\mathcal{C} \in [2, 4]$, which is more practical. Actually, the well-trained ArSSR model works for arbitrary up-sampling scale in the continuous interval \mathcal{C} . Here we only test the five discrete scales for convenience.

Figure 7 shows the qualitative comparison of all the compared models on a representative testing sample (No. #827035) from the testing set of the HCP-1200 dataset [43] for the SISR tasks of the five isotropic up-sampling scales $k = \{2, 2.5, 3, 3.5, 4\}$. To sum up, the ArSSR model produces the best SISR results in terms of image sharpness and HR fine details for all the scales. In particular, the SISR results from cubic interpolation are extremely blurry and with severe artifacts; while SRCNN3D [9], DCSRNN [10], and ResCNN [11] models recover limited fine details in HR image and their results get more blurred with the up-sample scale increasing. For example, as emphasized in the round dash mark, the narrow CSF between in the corti-

cal gyrus is only well recovered by the proposed model in each scaling rate. As shown in Figure 8, we select a red line on the axial view of the 3 \times SISR results (No. #531536) from all the comparison models to evaluate the reconstructed local image contrast. The SR result by the proposed ArSSR model has the sharpest changes in intensity profile line, which is the closest result compared with that in the GT image.

In Table 1, we demonstrate the quantitative results of all the compared models on the testing set of the HCP-1200 dataset [43] for the SISR tasks of the five isotropic up-sampling scales $k = \{2, 2.5, 3, 3.5, 4\}$. In terms of PSNR and SSIM [45], ResCNN [11] achieves the best performance for all the scale cases; while our ArSSR model only score higher than cubic interpolation. However, we need to emphasis that as claimed in [13, 21, 44], an over-smoothed SR result may score high on the two metrics. Therefore, the reason why SRCNN3D [9], DCSRNN [10], and ResCNN [11] achieve higher scores than the proposed ArSSR may be that they produced more smooth SISR results. In terms of LPIPS

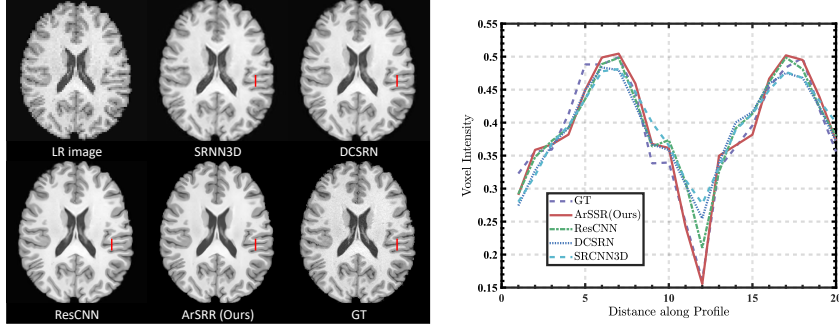


Figure 8: **Left Figure:** Qualitative comparison of all the compared models on a representative testing sample (No. #531536) from the testing set of the HCP-1200 dataset [43] for the SISR task of an isotropic up-sampling scale $k = 3$; **Right Figure:** Intensity profiles of the selected red lines on GT image and the SISR results.

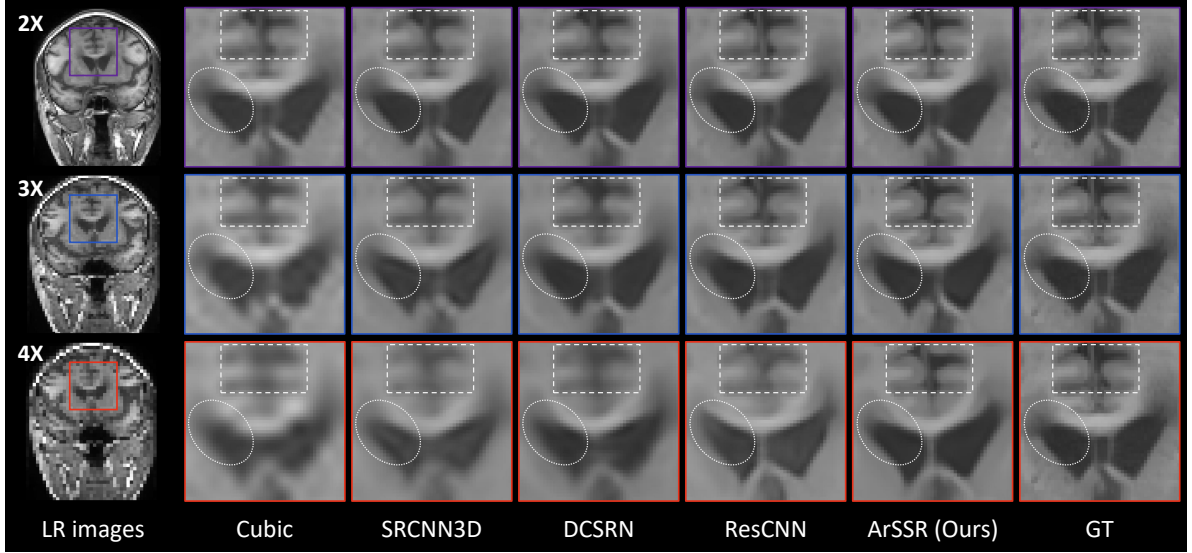


Figure 9: Qualitative comparison of all the compared models on a representative testing sample (No. #3) from the lesion brain dataset for the SISR tasks of an isotropic up-sampling scales $k = 3$. Note that here all the models are trained on the HCP-1200 dataset [43] and any fine-tuning is not employed.

[46], PSI [47], and LPC-SI [48], we observe that the ArSSR provides the best performance in most of the scale cases.

4.2.2. The SISR Tasks on the Lesion Brain Dataset

In order to further compare the generalization ability of the ArSSR model with the four baseline methods, we employ all the well-trained comparison models to perform the SISR tasks of three isotropic up-sampling scales $k = \{2, 3, 4\}$ on the Lesion Brain dataset for assessing the ability of recovering fine image detail that is not included in the training dataset. We need to emphasize that here all the compared model only trained on the HCP-1200 dataset [43] without any fine-tuning before testing on other dataset.

In figure 9, we demonstrate a qualitative comparison of all the compared models on a representative subject (No. #3) from the Lesion Brain dataset for the SISR tasks of the three isotropic up-sampling scales $k = \{2, 3, 4\}$. Effected by different MR scanner and image scanning parameter, the image contrast between Gray Matter (GM) and White Matter (WM) in this dataset is slightly different from that in the training dataset (HCP-1200 Dataset). Obviously, the SISR results from cubic interpolation are still with severe blocking artifacts. While the SISR results from the three deep-learning-based models dramatically become more blurry with the up-sampling scale increasing. For example, as indicated by the ellipse mark in figure 9, when scale rate $k = \{3, 4\}$ the WM lesion beside cerebrospinal fluid

Scales	Models	Reference-based Metrics			Non-reference-based Metrics	
		PSNR \uparrow	SSIM \uparrow	LPIPS \downarrow	PSI \uparrow	LCP-SI \uparrow
2 \times	Cubic	33.00 \pm 1.23	0.8362 \pm 0.1235	0.0471 \pm 0.0104	0.2402 \pm 0.0410	0.9650 \pm 0.0035
	SRCNN3D	34.56 \pm 0.86	0.9669 \pm 0.0044	0.0296 \pm 0.0071	0.2289 \pm 0.0471	0.9674 \pm 0.0041
	DCSRN	35.53 \pm 0.86	0.9777 \pm 0.0037	0.0187 \pm 0.0051	0.2317 \pm 0.0425	0.9693 \pm 0.0031
	ResCNN	35.70 \pm 0.90	0.9759 \pm 0.0036	0.0149 \pm 0.0045	0.2439 \pm 0.0396	0.9703 \pm 0.0030
	ArSSR (Ours)	31.27 \pm 0.78	0.9582 \pm 0.0062	0.0245 \pm 0.0050	0.2373 \pm 0.0395	0.9683 \pm 0.0042
3 \times	Cubic	28.36 \pm 0.96	0.8001 \pm 0.1053	0.1739 \pm 0.0249	0.2038 \pm 0.0298	0.9554 \pm 0.0056
	SRCNN3D	29.26 \pm 0.83	0.8206 \pm 0.0157	0.1006 \pm 0.0170	0.1898 \pm 0.0297	0.9556 \pm 0.0051
	DCSRN	30.01 \pm 0.89	0.9284 \pm 0.0099	0.0780 \pm 0.0143	0.2042 \pm 0.0371	0.9600 \pm 0.0039
	ResCNN	29.13 \pm 0.85	0.9125 \pm 0.0110	0.0617 \pm 0.0111	0.2408 \pm 0.0411	0.9678 \pm 0.0030
	ArSSR (Ours)	27.10 \pm 0.77	0.8975 \pm 0.0143	0.0603 \pm 0.0109	0.2507 \pm 0.0300	0.9678 \pm 0.0069
4 \times	Cubic	25.82 \pm 0.76	0.7508 \pm 0.0895	0.2798 \pm 0.0290	0.1711 \pm 0.0267	0.9430 \pm 0.0078
	SRCNN3D	26.35 \pm 0.77	0.8027 \pm 0.0213	0.1767 \pm 0.0217	0.1725 \pm 0.0232	0.9403 \pm 0.0084
	DCSRN	26.99 \pm 0.87	0.8588 \pm 0.0167	0.1580 \pm 0.0217	0.1869 \pm 0.0342	0.9519 \pm 0.0071
	ResCNN	25.95 \pm 0.86	0.8416 \pm 0.0203	0.1394 \pm 0.0191	0.2274 \pm 0.0377	0.9593 \pm 0.0046
	ArSSR (Ours)	25.16 \pm 0.75	0.8388 \pm 0.0214	0.1005 \pm 0.0170	0.2145 \pm 0.0322	0.9666 \pm 0.0072

Table 2: Quantitative results of all the compared models on the lesion brain dataset for the SISR tasks of the three isotropic up-sampling scales $k = \{2, 3, 4\}$. Note that all the models are trained on the HCP-1200 dataset [43] and any fine-tuning is not employed. The symbol \uparrow means that the higher score, the better image quality; while the symbol \downarrow indicates that the lower score, the better image quality. The best and second performance are highlighted in **red** and **blue**, respectively.

(CSF) is tended to merge into the CSF region in SR results of ResCNN and SRCNN3D, and in DCSRN the boundary of lesion and CSF is also very hard to be figured out. Besides, the image intensity become brighter in the CSF and the borders between CSF and GM are also blurred in the three deep-learning-based models. Only ArSSR model can produce sharp and clear image contrast between GM and WM, and between CSF and GM in the cortical regions (shown in the triangle mark) for all the three up-sampling scales.

Table 2 shows the quantitative results of all the compared models on the Lesion Brain dataset for the SISR tasks of the three isotropic up-sampling scales $k = \{2, 3, 4\}$. Similar to the quantitative result on the testing set of the HCP-1200 dataset [43], in terms of PSNR and SSIM, the proposed ArSSR model has low scores; while in terms of LPIPS [46], PSI [47], and LCP-SI [48], the ArSSR model obtain the best performance in the most of the scales. Although when $k = \{3, 4\}$ the contrasts of brain lesion are not as clear as in the GT, but the boundary between lesion, normal WM tissue and CSF are clearly distinguishable, while the contrast in of GM, WM and CSF are very clear in the triangle bound-box.

4.2.3. The SISR Tasks on the Healthy Brain Dataset

The Healthy Brain dataset consists of a LR input image and a HR reference image, we test the ArSSR model and two baseline methods (cubic interpolation and ResCNN [11]) for the SISR tasks of the three isotropic up-sampling scales $k = \{2, 3, 4\}$. Only the

qualitative results are reported because there are no GT HR images. Note that here ResCNN [11] and the ArSSR model are trained on the HCP-1200 dataset without any fine-tune before testing on other dataset.

Figure 10 demonstrates the qualitative comparison of cubic interpolation, ResCNN [11], and the ArSSR model on the Healthy Brain dataset for the SISR tasks of the three isotropic up-sampling scales $k = \{2, 3, 4\}$. From the visual inspection, the SISR images from cubic interpolation are blurry and rarely improved compared to the LR input image. ResCNN [11] and the ArSSR model produce similar SISR results in terms of both the image sharpness and HR fine details for all three scales. While for the reconstruction of fine image details, ArSSR model generates more consistent local image pattern in different up-sampling scales. As shown in the round marks in Figure 10, the CSF regions in-between cortical sulcus and gyrus are all clear in different scale SR result of ArSSR, and the local image patterns are highly similar; while in ResCNN, the clearness level of the CSF pattern carries among different up-sampling scales.

Benefitting from the large voxel size in LR image scanning, the SNR in each voxel of the LR input image is about 8 times higher than that in the reference HR image. Therefore, the image contrast between white matter and gray matter in the reconstructed images is much higher than that in the reference HR image. This result suggests two important notes: (a) the ArSSR is a more effective and reasonable method to acquire high-quality HR images comparing with scanning directly

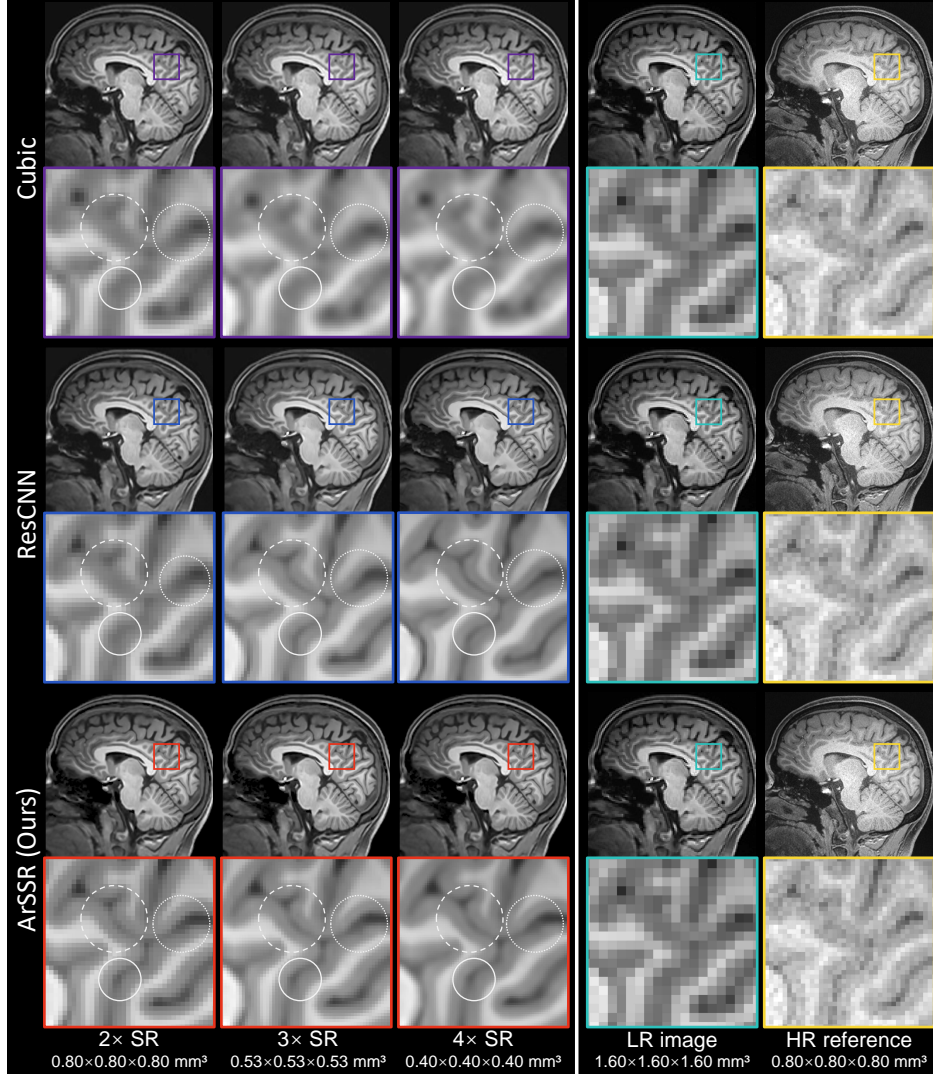


Figure 10: Qualitative comparison of LR input image, Reference image, SISR results by cubic interpolation, ResCNN [11], and ArSSR (Ours). Here three ResCNN [11] models and single ArSSR model are trained on the HCP-1200 dataset [43], and any fine-tuning is not employed.

low-SNR HR images; (b) Compared with the state-of-the-art deep-learning-based SR methods, the single ArSSR model can achieve a better performance for the SISR tasks with an arbitrary up-sampling scales, which can greatly improve practical applicability in MR image scanning.

4.2.4. Fully Automatic Segmentation based Evaluation

To further compare the quality of the SISR results from all the different deep learning models, we follow the segmentation evaluation strategy as in the previous work [8, 44]. Specifically, we use Ants (<http://stnava.github.io/ANTs/>), an open-source medical image processing tool, to conduct a fully

automatic segmentation on the GT images and all the SISR results. Each brain MR image is separated into six regions: CSF, GM, WM, Deep Gray Matter, Brain Stem, and Cerebellum. We quantitatively calculate the Dice Similarity Coefficient (Dice) [51] and Intersection over Union (IoU) [52] between the segmentations on the GT images and the SISR results.

Figure 11 shows the qualitative comparison of the fully automatic segmentation on a representative testing sample (No. #996782) in GT images and the $2\times$ SISR results of all the compared models. Note that Red, Blue, Yellow, Pink, Green and Cyan represent CSF, Gray Matter, Deep Gray Matter, Cerebellum, White Matter, and Brain Stem, respectively. All three views (Axial view,

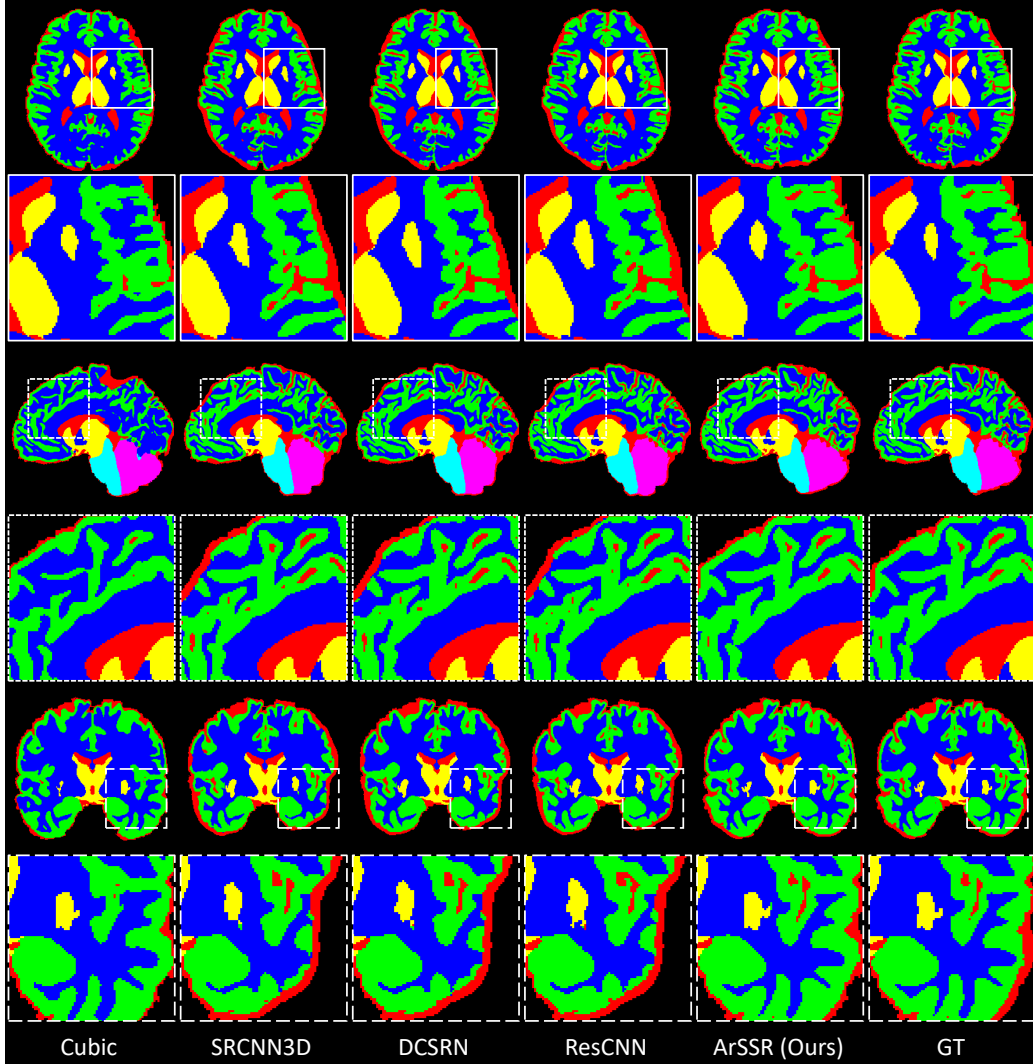


Figure 11: Qualitative comparison of the fully automatic segmentation on a representative testing sample (No. #996782) from the $2\times$ SISR results of all the compared models on the testing dataset of the HCP-1200 dataset [43].

Sagittal view, and Coronal view) clearly illustrate that compared with the baseline methods, the segmentation results of the ArSSR model are closest to those of the GT image.

Table 4 demonstrates the quantitative results of the fully automatic segmentation on the SISR results of all the compared models. Except for that when the scale $k = 4$, ResCNN [11] slightly outperforms the ArSSR model on the segmentation region of the White Matter (Dice [51]: 0.9317 vs 0.9284, IoU [52]: 0.8721 vs 0.8664), ArSSR achieves the best performance on all segmentation regions for all scales, which is consistent with the above-mentioned qualitative results.

4.2.5. Stability Analysis for the ArSSR Model

On the HCP-1200 dataset [43], we investigate the effect of the encoder network on the stability of the proposed model. we employ three different SISR models (ResCNN [11], SRResNet [21], and RDN [23]) to implement the encoder network. In order to match the dimension of the feature map produced by the encoder network, we modified the output channels of the three SISR models to 128. Same as the experiment #1, we qualitatively and quantitatively evaluate the performance of the ArSSR models with three different encoder networks for the SISR tasks of the five scales.

Figure 13 illustrates the qualitative comparison of

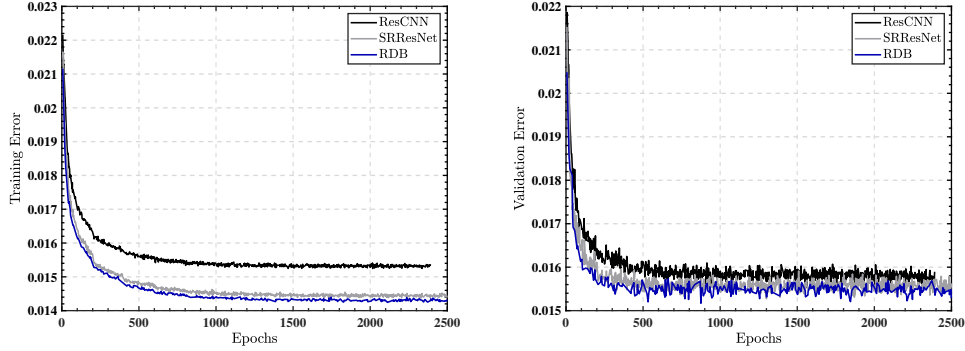


Figure 12: The curves of training error (**Left Figure**) and validation error (**Right Figure**) of the ArSSR models with three different encoder networks (ResCNN [11], SRResNet [21] and RDN [23]).

Scales	Encoder	Reference-based Metrics			Non-reference-based Metrics	
		PSNR \uparrow	SSIM \uparrow	LPIPS \downarrow	PSI \uparrow	LCP-SI \uparrow
2 \times	ResCNN	36.92 \pm 2.30	0.9722 \pm 0.0070	0.0573 \pm 0.0166	0.3010 \pm 0.0118	0.9435 \pm 0.0094
	SRResNet	36.59 \pm 2.24	0.9708 \pm 0.0070	0.0554 \pm 0.0161	0.2937 \pm 0.0121	0.9444 \pm 0.0090
	RDB	36.55 \pm 2.17	0.9700 \pm 0.0066	0.0549 \pm 0.0157	0.3083 \pm 0.0118	0.9435 \pm 0.0091
2.5 \times	ResCNN	35.17 \pm 2.31	0.9585 \pm 0.0094	0.0736 \pm 0.0192	0.3043 \pm 0.0125	0.9429 \pm 0.0101
	SRResNet	34.85 \pm 2.19	0.9562 \pm 0.0093	0.0730 \pm 0.0194	0.2910 \pm 0.0129	0.9435 \pm 0.0095
	RDB	34.57 \pm 2.11	0.9538 \pm 0.0087	0.0715 \pm 0.0187	0.3089 \pm 0.0120	0.9428 \pm 0.0095
3 \times	ResCNN	34.10 \pm 2.28	0.9485 \pm 0.0103	0.0841 \pm 0.0196	0.2862 \pm 0.0113	0.9434 \pm 0.0101
	SRResNet	33.81 \pm 2.15	0.9462 \pm 0.0100	0.0835 \pm 0.0195	0.2753 \pm 0.0115	0.9436 \pm 0.0100
	RDB	33.42 \pm 2.07	0.9426 \pm 0.0092	0.0811 \pm 0.0188	0.2986 \pm 0.0123	0.9426 \pm 0.0099
3.5 \times	ResCNN	32.77 \pm 2.26	0.9322 \pm 0.0121	0.1054 \pm 0.0219	0.2632 \pm 0.0115	0.9420 \pm 0.0111
	SRResNet	32.45 \pm 2.12	0.9295 \pm 0.0114	0.1034 \pm 0.0212	0.2486 \pm 0.0123	0.9427 \pm 0.0109
	RDB	31.98 \pm 2.04	0.9242 \pm 0.0106	0.1009 \pm 0.0212	0.2798 \pm 0.0115	0.9405 \pm 0.0111
4 \times	ResCNN	32.18 \pm 2.26	0.9240 \pm 0.0125	0.1187 \pm 0.0220	0.2345 \pm 0.0101	0.9404 \pm 0.0115
	SRResNet	31.86 \pm 2.11	0.9220 \pm 0.0115	0.1161 \pm 0.0214	0.2220 \pm 0.0092	0.9411 \pm 0.0115
	RDB	31.33 \pm 2.03	0.9155 \pm 0.0107	0.1136 \pm 0.0215	0.2534 \pm 0.0090	0.9394 \pm 0.0114

Table 3: Quantitative results of the ArSSR models with three different encoder networks (RDN [23], ResCNN [11], SRResNet [21]) on the testing set of the HCP-1200 dataset [43] for the SISR tasks of the five isotropic up-sampling scales $k = \{2, 2.5, 3, 3.5, 4\}$. The symbol \uparrow means that the higher score, the better image quality; while the symbol \downarrow indicates that the lower score, the better image quality. The best performance is highlighted in **bold**.

the ArSSR models with the three different encoder networks on a representative testing sample (No. #531536) from the testing set of the HCP-1200 dataset [43] for the SISR task of an isotropic up-sampling scale $k = 2$. We observe that, compared with the GT image, all the SISR results are less noisy and almost have the same HR fine details, which indicates that the encoder network module does not significantly affect the ArSSR model for the SISR tasks. As depicted in Figure 12, the training error curves and validation error curves of the ArSSR models with the three different encoder networks are similar greatly, which indicates that the ArSSR has strong stability for the model training.

In Table 3, we demonstrate the quantitative results of the ArSSR models with the three different encoder

networks on the testing set of the HCP-1200 [43] for the SISR tasks of the five isotropic up-sampling scales $k = \{2, 2.5, 3, 3.5, 4\}$. In terms of PSNR and SSIM [45], the ArSSR model with the ResCNN [11] encoder network achieves the highest scores for all the scales. In terms of LPIPS [46] and PSI [47], the ArSSR model with the RDN [23] encoder network obtains the best performance for all the scales. While for LPC-SI [48], the ArSSR model with the SRResNet [21] encoder network produces the highest scores for all the scales. In summary, the three models achieve very close SR performance. These quantitative results further suggest that the ArSSR model is not significantly affected by the encoder network module.

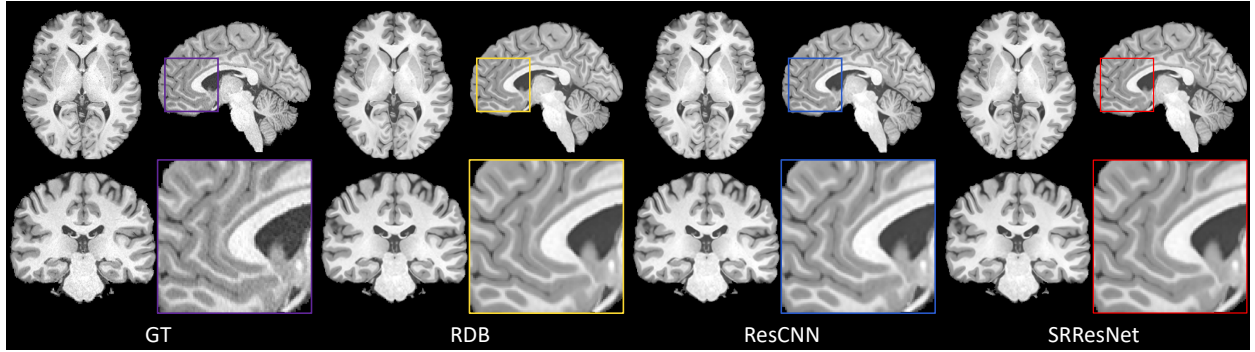


Figure 13: Qualitative comparison of the ArSSR models with three different encoder networks (RDN [23], ResCNN [11], and SRResNet [21]) on a representative testing sample (No. #531536) from the testing set of the HCP-1200 dataset [43] for the SISR task of an isotropic up-sampling scale $k = 2$.

5. Conclusion

In the paper, we proposed ArSSR model to conduct SISR tasks of arbitrary up-sampling scales for 3D MR images. In our model, a novel continuous implicit voxel function was used to represent the pairs of LR-HR images in the SISR tasks. By combining a convolutional encoder with the continuous implicit voxel function, the well-trained single ArSSR model was able to recover the HR image of arbitrary resolution from an unknown LR input image. The results from experiments on the two simulation datasets (a large public dataset with 1113 subjects and a small lesion brain dataset with 17 subjects) showed that for the SISR tasks of several different up-sampling scales, the single ArSSR model outperformed other popular CNNs-based methods in terms of both the HR fine details and image sharpness. And on the real collected dataset, the SISR results from the single ArSSR model provided finer anatomical details and sharper image contrast compared to the HR reference image with low SNR, which demonstrated that our ArSSR model was capable for more broad real scene applications. In summary, the single ArSSR model based on the implicit neural representation could conduct the reconstruction of HR images at arbitrary scales, which would substantially improve the practicality of HR MRI.

References

- [1] Y. Jia, A. Gholipour, Z. He, S. K. Warfield, A new sparse representation framework for reconstruction of an isotropic high spatial resolution mr volume from orthogonal anisotropic resolution scans, *IEEE transactions on medical imaging* 36 (5) (2017) 1182–1193.
- [2] B. Scherrer, A. Gholipour, S. K. Warfield, Super-resolution reconstruction to increase the spatial resolution of diffusion
- weighted images from orthogonal anisotropic acquisitions, *Medical image analysis* 16 (7) (2012) 1465–1476.
- [3] Z. Wang, J. Chen, S. C. Hoi, Deep learning for image super-resolution: A survey, *IEEE transactions on pattern analysis and machine intelligence*.
- [4] S. Peled, Y. Yeshurun, Superresolution in mri: application to human white matter fiber tract visualization by diffusion tensor imaging, *Magnetic Resonance in Medicine: An Official Journal of the International Society for Magnetic Resonance in Medicine* 45 (1) (2001) 29–35.
- [5] M. Ebner, G. Wang, W. Li, M. Aertsen, P. A. Patel, R. Aughwane, A. Melbourne, T. Doel, S. Dymarkowski, P. De Coppi, et al., An automated framework for localization, segmentation and super-resolution reconstruction of fetal brain mri, *NeuroImage* 206 (2020) 116324.
- [6] F. Shi, J. Cheng, L. Wang, P.-T. Yap, D. Shen, Lrtv: Mr image super-resolution with low-rank and total variation regularizations, *IEEE transactions on medical imaging* 34 (12) (2015) 2459–2466.
- [7] A. Rueda, N. Malpica, E. Romero, Single-image super-resolution of brain mr images using overcomplete dictionaries, *Medical image analysis* 17 (1) (2013) 113–132.
- [8] Y. Chen, A. G. Christodoulou, Z. Zhou, F. Shi, Y. Xie, D. Li, Mri super-resolution with gan and 3d multi-level densenet: smaller, faster, and better, *arXiv preprint arXiv:2003.01217*.
- [9] C.-H. Pham, A. Ducournau, R. Fablet, F. Rousseau, Brain mri super-resolution using deep 3d convolutional networks, in: 2017 IEEE 14th International Symposium on Biomedical Imaging (ISBI 2017), IEEE, 2017, pp. 197–200.
- [10] Y. Chen, Y. Xie, Z. Zhou, F. Shi, A. G. Christodoulou, D. Li, Brain mri super resolution using 3d deep densely connected neural networks, in: 2018 IEEE 15th International Symposium on Biomedical Imaging (ISBI 2018), IEEE, 2018, pp. 739–742.
- [11] J. Du, Z. He, L. Wang, A. Gholipour, Z. Zhou, D. Chen, Y. Jia, Super-resolution reconstruction of single anisotropic 3d mr images using residual convolutional neural network, *Neurocomputing* 392. doi:10.1016/j.neucom.2018.10.102.
- [12] Q. Delannoy, C.-H. Pham, C. Cazorla, C. Tor-Díez, G. Dollé, H. Meunier, N. Bednarek, R. Fablet, N. Passat, F. Rousseau, Segsrgan: Super-resolution and segmentation using generative adversarial networks—application to neonatal brain mri, *Computers in Biology and Medicine* 120 (2020) 103755.
- [13] Y. Chen, F. Shi, A. G. Christodoulou, Y. Xie, Z. Zhou, D. Li, Efficient and accurate mri super-resolution using a generative adversarial network and 3d multi-level densely connected network,

Scales	Segmentation Regions	Cubic	SRCNN3D	DCSRN	ResCNN	ArSSR (Ours)
2×	CSF	0.6857/0.5239	0.6840/0.5203	0.6806/0.5164	0.6816/0.5176	0.9065/0.8293
	Gray Matter	0.7285/0.5850	0.8639/0.7605	0.8636/0.7601	0.8650/0.7622	0.9491/0.9033
	White Matter	0.8499/0.7435	0.9510/0.9067	0.9512/0.9070	0.9517/0.9079	0.9739/0.9492
	Deep Gray Matter	0.8896/0.8050	0.9499/0.9046	0.9510/0.9066	0.9508/0.9063	0.9751/0.9515
	Brain Stem	0.9137/0.8447	0.9561/0.9162	0.9560/0.9159	0.9557/0.9154	0.9804/0.9617
	Cerebellum	0.8640/0.7676	0.8465/0.7341	0.8456/0.7329	0.8476/0.7358	0.9776/0.9564
	Total Means	0.8219/0.7116	0.8752/0.7904	0.8747/0.7898	0.8754/0.7909	0.9604/0.9252
2.5×	CSF	0.7362/0.5843	0.6731/0.5079	0.6750/0.5100	0.6746/0.5096	0.8797/0.7854
	Gray Matter	0.7854/0.6527	0.8527/0.7433	0.8554/0.7475	0.8608/0.7557	0.9294/0.8681
	White Matter	0.8796/0.7876	0.9454/0.8964	0.9475/0.9003	0.9503/0.9053	0.9626/0.9279
	Deep Gray Matter	0.9070/0.8317	0.9400/0.8868	0.9440/0.8939	0.9472/0.8998	0.9620/0.9270
	Brain Stem	0.9378/0.8843	0.9591/0.9216	0.9603/0.9238	0.9595/0.9224	0.9806/0.9619
	Cerebellum	0.9066/0.8320	0.8476/0.7357	0.8495/0.7386	0.8502/0.7396	0.9723/0.9462
	Total Means	0.8588/0.7621	0.8696/0.7819	0.8720/0.7857	0.8738/0.7887	0.9478/0.9028
3×	CSF	0.7009/0.5411	0.6663/0.5002	0.6692/0.5035	0.6714/0.5060	0.8570/0.7500
	Gray Matter	0.7603/0.6191	0.8377/0.7209	0.8480/0.7362	0.8559/0.7483	0.9118/0.8380
	White Matter	0.8665/0.7667	0.9352/0.8784	0.9414/0.8893	0.9457/0.8971	0.9526/0.9095
	Deep Gray Matter	0.8926/0.8079	0.9292/0.8679	0.9350/0.8780	0.9370/0.8816	0.9519/0.9083
	Brain Stem	0.9270/0.8659	0.9514/0.9075	0.9522/0.9089	0.9533/0.9109	0.9711/0.9439
	Cerebellum	0.8883/0.8027	0.8401/0.7246	0.8401/0.7246	0.8434/0.7294	0.9653/0.9331
	Total Means	0.8393/0.7339	0.8600/0.7666	0.8643/0.7734	0.8678/0.7789	0.9350/0.8805
3.5×	CSF	0.7337/0.5803	0.6548/0.4874	0.6605/0.4937	0.6523/0.4846	0.8308/0.7107
	Gray Matter	0.7932/0.6609	0.8178/0.6919	0.8323/0.7129	0.8422/0.7276	0.8909/0.8033
	White Matter	0.8860/0.7969	0.9236/0.8582	0.9338/0.8758	0.9397/0.8863	0.9406/0.8879
	Deep Gray Matter	0.8972/0.8148	0.9115/0.8375	0.9212/0.8540	0.9303/0.8697	0.9404/0.8877
	Brain Stem	0.9415/0.8901	0.9537/0.9117	0.9549/0.9139	0.9551/0.9142	0.9712/0.9441
	Cerebellum	0.9126/0.8409	0.8416/0.7267	0.8430/0.7287	0.8438/0.7300	0.9636/0.9299
	Total Means	0.8607/0.7640	0.8505/0.7522	0.8576/0.7632	0.8606/0.7687	0.9229/0.8606
4×	CSF	0.6957/0.5344	0.6461/0.4779	0.6581/0.4911	0.6516/0.4839	0.8062/0.6756
	Gray Matter	0.7601/0.6167	0.7967/0.6622	0.8247/0.7018	0.8312/0.7113	0.8709/0.7714
	White Matter	0.8675/0.7674	0.9095/0.8341	0.9242/0.8592	0.9317/0.8721	0.9284/0.8664
	Deep Gray Matter	0.8813/0.7892	0.8962/0.8121	0.9121/0.8386	0.9217/0.8550	0.9291/0.8679
	Brain Stem	0.9265/0.8642	0.9436/0.8936	0.9470/0.8997	0.9497/0.9046	0.9618/0.9266
	Cerebellum	0.8862/0.7978	0.8340/0.7155	0.8378/0.7211	0.8384/0.7221	0.9529/0.9102
	Total Means	0.8362/0.7283	0.8377/0.7326	0.8506/0.7519	0.8540/0.7582	0.9082/0.8364

Table 4: Quantitative results (Dice [51] and IoU [52]) of the fully automatic segmentation on the SISR results of all the compared models on the testing dataset of the HCP-1200 dataset [43]. Note that SRCNN3D [9], DCSRNN [10], and ResCNN [11] are *respectively* trained and tested for each scale; while a *single* ArSSR (Ours) model is trained and tested for the five scales. The best and second performance are highlighted in **red** and **blue**, respectively.

- in: International Conference on Medical Image Computing and Computer-Assisted Intervention, Springer, 2018, pp. 91–99.
- [14] Q. Lyu, H. Shan, C. Steber, C. Helis, C. Whitlow, M. Chan, G. Wang, Multi-contrast super-resolution mri through a progressive network, IEEE transactions on medical imaging 39 (9) (2020) 2738–2749.
- [15] W.-C. Siu, K.-W. Hung, Review of image interpolation and super-resolution, in: Proceedings of The 2012 Asia Pacific Signal and Information Processing Association Annual Summit and Conference, IEEE, 2012, pp. 1–10.
- [16] L. I. Rudin, S. Osher, E. Fatemi, Nonlinear total variation based noise removal algorithms, Physica D: nonlinear phenomena 60 (1-4) (1992) 259–268.
- [17] C. Dong, C. C. Loy, K. He, X. Tang, Learning a deep convolutional network for image super-resolution, in: European conference on computer vision, Springer, 2014, pp. 184–199.
- [18] C. Dong, C. C. Loy, K. He, X. Tang, Image super-resolution using deep convolutional networks, IEEE transactions on pattern analysis and machine intelligence 38 (2) (2015) 295–307.
- [19] B. Lim, S. Son, H. Kim, S. Nah, K. Mu Lee, Enhanced deep residual networks for single image super-resolution, in: Proceedings of the IEEE conference on computer vision and pattern recognition workshops, 2017, pp. 136–144.
- [20] J. Kim, J. K. Lee, K. M. Lee, Accurate image super-resolution using very deep convolutional networks, in: Proceedings of the IEEE conference on computer vision and pattern recognition, 2016, pp. 1646–1654.
- [21] C. Ledig, L. Theis, F. Huszár, J. Caballero, A. Cunningham, A. Acosta, A. Aitken, A. Tejani, J. Totz, Z. Wang, et al., Photo-realistic single image super-resolution using a generative adversarial network, in: Proceedings of the IEEE conference on computer vision and pattern recognition, 2017, pp. 4681–4690.
- [22] W. Shi, J. Caballero, F. Huszár, J. Totz, A. P. Aitken, R. Bishop, D. Rueckert, Z. Wang, Real-time single image and video super-resolution using an efficient sub-pixel convolutional neural network, in: Proceedings of the IEEE conference on computer vi-

- sion and pattern recognition, 2016, pp. 1874–1883.
- [23] Y. Zhang, Y. Tian, Y. Kong, B. Zhong, Y. Fu, Residual dense network for image super-resolution, in: Proceedings of the IEEE conference on computer vision and pattern recognition, 2018, pp. 2472–2481.
 - [24] C. Ma, Y. Rao, Y. Cheng, C. Chen, J. Lu, J. Zhou, Structure-preserving super resolution with gradient guidance, in: Proceedings of the IEEE/CVF Conference on Computer Vision and Pattern Recognition, 2020, pp. 7769–7778.
 - [25] J. Kim, J. K. Lee, K. M. Lee, Deeply-recursive convolutional network for image super-resolution, in: Proceedings of the IEEE conference on computer vision and pattern recognition, 2016, pp. 1637–1645.
 - [26] W.-S. Lai, J.-B. Huang, N. Ahuja, M.-H. Yang, Deep laplacian pyramid networks for fast and accurate super-resolution, in: Proceedings of the IEEE conference on computer vision and pattern recognition, 2017, pp. 624–632.
 - [27] Z. Chen, H. Zhang, Learning implicit fields for generative shape modeling, in: Proceedings of the IEEE/CVF Conference on Computer Vision and Pattern Recognition, 2019, pp. 5939–5948.
 - [28] J. J. Park, P. Florence, J. Straub, R. Newcombe, S. Lovegrove, Deepsdf: Learning continuous signed distance functions for shape representation, in: Proceedings of the IEEE/CVF Conference on Computer Vision and Pattern Recognition, 2019, pp. 165–174.
 - [29] L. Mescheder, M. Oechsle, M. Niemeyer, S. Nowozin, A. Geiger, Occupancy networks: Learning 3d reconstruction in function space, in: Proceedings of the IEEE/CVF Conference on Computer Vision and Pattern Recognition, 2019, pp. 4460–4470.
 - [30] S. Peng, M. Niemeyer, L. Mescheder, M. Pollefeys, A. Geiger, Convolutional occupancy networks, in: Computer Vision—ECCV 2020: 16th European Conference, Glasgow, UK, August 23–28, 2020, Proceedings, Part III 16, Springer, 2020, pp. 523–540.
 - [31] B. Mildenhall, P. P. Srinivasan, M. Tancik, J. T. Barron, R. Ramamoorthi, R. Ng, Nerf: Representing scenes as neural radiance fields for view synthesis, in: European conference on computer vision, Springer, 2020, pp. 405–421.
 - [32] A. Yu, V. Ye, M. Tancik, A. Kanazawa, pixelnerf: Neural radiance fields from one or few images, in: Proceedings of the IEEE/CVF Conference on Computer Vision and Pattern Recognition, 2021, pp. 4578–4587.
 - [33] L. Liu, J. Gu, K. Zaw Lin, T.-S. Chua, C. Theobalt, Neural sparse voxel fields, *Advances in Neural Information Processing Systems* 33.
 - [34] K. Park, U. Sinha, J. T. Barron, S. Bouaziz, D. B. Goldman, S. M. Seitz, R. Martin-Brualla, Nerfies: Deformable neural radiance fields, in: Proceedings of the IEEE/CVF International Conference on Computer Vision, 2021, pp. 5865–5874.
 - [35] S. Peng, Y. Zhang, Y. Xu, Q. Wang, Q. Shuai, H. Bao, X. Zhou, Neural body: Implicit neural representations with structured latent codes for novel view synthesis of dynamic humans, in: Proceedings of the IEEE/CVF Conference on Computer Vision and Pattern Recognition, 2021, pp. 9054–9063.
 - [36] Y. Chen, S. Liu, X. Wang, Learning continuous image representation with local implicit image function, in: Proceedings of the IEEE/CVF Conference on Computer Vision and Pattern Recognition, 2021, pp. 8628–8638.
 - [37] C. H. Lin, H.-Y. Lee, Y.-C. Cheng, S. Tulyakov, M.-H. Yang, Infinitygan: Towards infinite-resolution image synthesis, *arXiv preprint arXiv:2104.03963*.
 - [38] J. Tang, X. Chen, G. Zeng, Joint implicit image function for guided depth super-resolution, *arXiv preprint arXiv:2107.08717*.
 - [39] Q. Wu, Y. Li, L. Xu, R. Feng, H. Wei, Q. Yang, B. Yu, X. Liu, J. Yu, Y. Zhang, Irem: High-resolution magnetic resonance image reconstruction via implicit neural representation, in: International Conference on Medical Image Computing and Computer-Assisted Intervention, Springer, 2021, pp. 65–74.
 - [40] D. E. Rumelhart, G. E. Hinton, R. J. Williams, Learning representations by back-propagating errors, *nature* 323 (6088) (1986) 533–536.
 - [41] K. He, X. Zhang, S. Ren, J. Sun, Delving deep into rectifiers: Surpassing human-level performance on imagenet classification, *IEEE International Conference on Computer Vision (ICCV 2015)* 1502. doi:10.1109/ICCV.2015.123.
 - [42] K. He, X. Zhang, S. Ren, J. Sun, Deep residual learning for image recognition, in: Proceedings of the IEEE conference on computer vision and pattern recognition, 2016, pp. 770–778.
 - [43] D. Van Essen, S. Smith, D. Barch, T. Behrens, E. Yacoub, K. Ugurbil, The wu-minn human connectome project: an overview, *NeuroImage* 80. doi:10.1016/j.neuroimage.2013.05.041.
 - [44] J. Wang, Y. Chen, Y. Wu, J. Shi, J. Gee, Enhanced generative adversarial network for 3d brain mri super-resolution, in: Proceedings of the IEEE/CVF Winter Conference on Applications of Computer Vision, 2020, pp. 3627–3636.
 - [45] Z. Wang, A. C. Bovik, H. R. Sheikh, E. P. Simoncelli, Image quality assessment: from error visibility to structural similarity, *IEEE transactions on image processing* 13 (4) (2004) 600–612.
 - [46] R. Zhang, P. Isola, A. A. Efros, E. Shechtman, O. Wang, The unreasonable effectiveness of deep features as a perceptual metric, in: Proceedings of the IEEE conference on computer vision and pattern recognition, 2018, pp. 586–595.
 - [47] C. Feichtenhofer, H. Fossold, P. Schallauer, A perceptual image sharpness metric based on local edge gradient analysis, *IEEE Signal Processing Letters* 20 (4) (2013) 379–382.
 - [48] R. Hassen, Z. Wang, M. M. Salama, Image sharpness assessment based on local phase coherence, *IEEE Transactions on Image Processing* 22 (7) (2013) 2798–2810.
 - [49] D. P. Kingma, J. Ba, Adam: A method for stochastic optimization, *CoRR abs/1412.6980*.
 - [50] P. Virtanen, R. Gommers, T. E. Oliphant, M. Haberland, T. Reddy, D. Cournapeau, E. Burovski, P. Peterson, W. Weckesser, J. Bright, et al., Scipy 1.0: fundamental algorithms for scientific computing in python, *Nature methods* 17 (3) (2020) 261–272.
 - [51] T. Sorensen, Method of establishing groups of equal amplitude in plant sociology based on similarity of species content and its application to analyses of the vegetation on danish commons, *Biol. Skr Dan Vid Sel.* 5.
 - [52] P. Jaccard, Etude de la distribution florale dans une portion des alpes et du jura, *Bulletin de la Societe Vaudoise des Sciences Naturelles* 37 (1901) 547–579. doi:10.5169/seals-266450.